Transport properties of heterogeneous materials derived from Gaussian random fields: Bounds and simulation

A. P. Roberts

Department of Applied Mathematics, Research School of Physical Sciences, Australian National University, Canberra, Australian Capital Territory, 0200 Australia

Max Teubner

Max-Planck-Institut für Biophysikalische Chemie, Postfach 2841, 3400 Göttingen, Federal Republic of Germany
(Received 8 September 1994)

We investigate the effective conductivity (σ_e) of a class of amorphous media defined by the level cut of a Gaussian random field. The three point solid-solid correlation function is derived and utilized in the evaluation of the Beran-Milton bounds. Simulations are used to calculate σ_e for a variety of fields and volume fractions at several different conductivity contrasts. Relatively large differences in σ_e are observed between the Gaussian media and the identical overlapping sphere model used previously as a "model" amorphous medium. In contrast, σ_e shows little variability between different Gaussian media.

PACS number(s): 05.40.+j, 72.15.Cz

I. INTRODUCTION

The calculation of the effective transport properties of random composite media is important in many scientific and engineering applications [1]. Several techniques (effective medium approximations and cluster expansions) have been developed for predicting the effective properties of such materials (briefly reviewed in Ref. [2]). However, difficulties encountered in such methods have provided the impetus for the development of rigorous bounds [3–8]. Such bounds rely on statistical descriptions of the microstructure of the material which are available for relatively few classes of media. The advancement of computing technology [9–12] has also made direct simulation of effective properties feasible. It is the latter two approaches which we shall discuss here, in the context of the effective conductivity of a three dimensional (3D) amorphous isotropic two phase material.

There have been significant advances in the evaluation of the Beran-Milton [4,7] (BM) bounds in the past decade. The key parameter ζ_1 (or $\zeta_2 = 1 - \zeta_1$) which incorporates microstructural information regarding the composite has been evaluated primarily for materials comprised of statistically independent cells [13,14] or dispersions of regularly shaped inclusions [15,16,2,17]. The simulation of the effective conductivity of continuum random media is a computationally intensive process and has only recently been studied for the second class of materials [10,11]. Such an approach provides a basis for testing the bounding theories and for generating outright predictions of the effective properties of composites.

A class of materials which is not, in general, well described by cellular or particulate models is that of amorphous composites. Such materials arise in certain alloys [18,19], microemulsions [20,21], and other systems [22]. The model which best captures some of the salient features of such composites is the spatially uncorrelated pen-etrable sphere (or the identical overlapping sphere) model [23]. Due to the simplicity in evaluating the statistical correlation functions of such a material it has served as a useful "model" amorphous medium [24,15,25]. However, specific features of this model restrict its generality. The inclusion (sphere) phase and the matrix phase are topologically very different, the small scale structure of the phase boundaries is spherical, and there are no long range correlations in the model. An alternative approach is to empirically measure the specific correlation functions of a sample and to apply the results in the evaluation of bounds [26,18,27,28]. This approach is complicated and subject to error. It is therefore interesting to seek a more complex model of amorphous composites, yet simple enough so that the correlation functions can be calculated.

Another method of modeling random composites is to define the interface between the phases as a level cut of some random field [29–33] (see Ref. [34] for a review). Recent progress [35–37] in the theory of interfaces of level-cut Gaussian random fields has made it possible to calculate the statistical information necessary for the evaluation of the BM bounds. There is evidence that the Gaussian random interface model is a good approximation to certain oil-water microemulsions [38,39,21] and we conjecture that it is a reasonable model for amorphous alloys.

In this paper we investigate the effective conductivity of such media using the above mentioned bounding techniques and computer simulations. The results are compared with the previously studied models to demonstrate the differences that arise. The paper is organized as follows. In Sec. II we describe the equations governing the electric field in a composite medium and the bounds on the effective conductivity. In Secs. III and IV we derive the statistical correlation functions for the random media and apply them in the calculation of the microstructure parameter. Sections V–VII are concerned with the gen-

eration of the random materials, the simulation of the effective conductivity, and comparison of the data with the bounds.

II. BOUNDS ON THE EFFECTIVE PROPERTIES OF COMPOSITE MATERIALS

The relationship between the current density j and the electric field $E = -\nabla\phi$ is given by Ohms law,

$$\mathbf{j} = -\sigma\nabla\phi, \tag{2.1}$$

where, due to charge conservation, ϕ satisfies

$$\nabla^2\phi = 0 \tag{2.2}$$

throughout the material. At the boundary of different regions of the material with conductivities σ_1 and σ_2 we have

$$\phi_1 = \phi_2, \quad \sigma_1\nabla\phi_1 \cdot \mathbf{n} = \sigma_2\nabla\phi_2 \cdot \mathbf{n}. \tag{2.3}$$

The effective conductivity is defined by a macroscopic form of Ohm's law,

$$\sigma_e = \frac{\langle\sigma\nabla\phi\rangle}{\langle\nabla\phi\rangle}. \tag{2.4}$$

Now consider a composite material made up of two components with conductivities σ_1 and σ_2 with volume fractions p and $q = 1-p$. The effective conductivity will then depend on the σ_i, their respective volume fractions, and the spatial distribution (microstructure) of each phase [40].

The first bounds on σ_e were calculated by Wiener [41] who proved that $\langle\sigma^{-1}\rangle^{-1} \leq \sigma_e \leq \langle\sigma\rangle$. These bounds assume no details about the microstructure and are hence valid for a general composite. As more statistical information regarding the composite is included in the calculation of the bounds they become more restrictive. If the sample is assumed to be isotropic and macroscopically homogeneous then the second order bounds of Hashin and Sthrikman [3] are applicable. To distinguish between such materials the third order bounds of Beran are necessary. [The term nth order bounds refers to the fact that the bounds are exact to $O(\sigma_1 - \sigma_2)^n$.] The Beran [4] bounds were derived using variational principles and were subsequently simplified by Milton [7]. Following the notation of Milton we define $\langle a\rangle = pa_1 + qa_2$, $\langle\tilde{a}\rangle = qa_1 + pa_2$ (interchanging p and q), and $\langle a\rangle_\zeta = \zeta_1 a_1 + \zeta_2 a_2$. Here $a_i = \sigma_i$ or $1/\sigma_i$. In these terms the lower bound on σ_e is

$$\sigma_l = \left[\langle\sigma^{-1}\rangle - \frac{2pq(\sigma_1^{-1} - \sigma_2^{-1})^2}{2\langle\tilde{\sigma}^{-1}\rangle + \langle\sigma^{-1}\rangle_\zeta}\right]^{-1} \tag{2.5}$$

while the upper bound is

$$\sigma_u = \left[\langle\sigma\rangle - \frac{pq(\sigma_1 - \sigma_2)^2}{\langle\tilde{\sigma}\rangle + 2\langle\sigma\rangle_\zeta}\right]. \tag{2.6}$$

The so called microstructure parameter ζ_1 is given by a number of equivalent integrals [4,7,14], of which the formulation due to Brown [40] is the best for our purposes,

$$\zeta_1 = \frac{9}{2pq}\int_0^\infty\frac{dr}{r}\int_0^\infty\frac{ds}{s}\int_{-1}^1 du P_2(u)$$
$$\times \left(p_3(r,s,t) - \frac{p_2(r)p_2(s)}{p}\right), \tag{2.7}$$

where $t^2 = r^2 + s^2 - 2rsu$ and $P_2(u) = (3u^2 - 1)/2$ is the Legendre polynomial of order 2. The functions p_n are n-point solid-solid correlation functions (see Sec. III) where the "solid" is phase 1 and the "void" is phase 2.

As Milton notes these bounds converge when $\zeta_1 = 0, 1$ and are equal to one of the second order Hashin-Sthrikman bounds in each case. An improved lower bound has been derived by Milton [8] for the case $\sigma_2 > \sigma_1$. In later sections we consider materials with $\sigma_1 > \sigma_2$ for which this bound is (see Ref. [11]), by interchanging the roles of the materials,

$$\sigma_l = \sigma_2\frac{1 + (1 + 2p)\beta_{12} - 2(q\zeta_1 - p)\beta_{12}^2}{1 + q\beta_{12} - (2q\zeta_1 + p)\beta_{12}^2}, \tag{2.8}$$

where $\beta_{12} = (\sigma_1 - \sigma_2)/(\sigma_1 + 2\sigma_2)$. By way of mathematical analogy these bounds also apply to the effective dielectric, diffusion and magnetic permeability coefficients of composite materials.

III. CORRELATION FUNCTIONS FOR THE GAUSSIAN RANDOM INTERFACE MODEL

There is an extensive literature on the calculation of statistical correlation functions [1]. The case of the three point solid-solid correlation function has been considered empirically [26,18,42,43], and theoretically for cellular materials [13,44] and spherical inclusions [23,15,16,45] to name a few. Here we take the interface between the phases to be defined by a level cut of a random field [29,31]. Now consider a Gaussian random field $y(\mathbf{r})$ [46,34] (see Sec. V) and let the level sets $y(\mathbf{r}) = \alpha$ define the interface (with the region $y > \alpha$ being phase 1). Then the n point correlation function is given by the volume average,

$$p_n(\mathbf{r}_1, \mathbf{r}_2, \ldots, \mathbf{r}_n) = \langle H(y_1 - \alpha)\ldots H(y_n - \alpha)\rangle, \tag{3.1}$$

where $H(y)$ is the Heaviside function and $y_i = y(\mathbf{r}_i)$. p_n is then the probability that the n points will lie in phase 1. For a macroscopically homogeneous isotropic material p_n only depends on the distances $r_{ij} = |\mathbf{r}_i - \mathbf{r}_j|$ between the points. Since volume and ensemble averages are equivalent in such a medium [40] we can use the latter to evaluate Eq. (3.1). The joint probability density of y_i is

$$P_n(y_1 y_2 \ldots y_n) = \frac{1}{\sqrt{(2\pi)^n|G|}}\exp(-\tfrac{1}{2}\mathbf{y}^T G^{-1}\mathbf{y}), \tag{3.2}$$

where the elements of G are $g_{ij} = \langle y_i y_j\rangle$ [46]. The latter quantity we refer to as the field-field correlation function,

$$g_{ij} = \int_0^\infty 4\pi k^2\rho(k)\frac{\sin k|\mathbf{r}_i - \mathbf{r}_j|}{k|\mathbf{r}_i - \mathbf{r}_j|}dk, \tag{3.3}$$

where $\rho(k)$ is the spectral density of the field.

Berk [35,37] and Teubner [36] have derived the one point function (volume fraction),

$$p = \frac{1}{\sqrt{2\pi}} \int_\alpha^\infty \exp(-\tfrac{1}{2}t^2)dt \qquad (3.4)$$

and the two point function,

$$p_2(g_{ij}) = \frac{1}{2\pi} \int_0^{g_{ij}} \exp\left(-\frac{\alpha^2}{1+t}\right) \frac{dt}{\sqrt{1-t^2}} + p^2. \qquad (3.5)$$

The three point function is calculated using the techniques described in Ref. [36]. The following identities are used [46]:

$$\langle \exp(i\mathbf{y} \cdot \mathbf{w}) \rangle = \exp(-\tfrac{1}{2}\mathbf{w}^T G \mathbf{w}) \qquad (3.6)$$

and

$$H(y-\alpha) = \frac{-1}{2\pi i} \int_C e^{-iw(y-\alpha)} \frac{dw}{w}, \qquad (3.7)$$

where the contour C is directed along the real axis except near the origin where it crosses the imaginary axis in the upper half plane. This leads (after algebra) to

$$\frac{\partial p_3^T}{\partial g_{12}} = \frac{\partial p_2(g_{12})}{\partial g_{12}} \frac{1}{\sqrt{2\pi}} \int_{\alpha F_{12}}^\alpha \exp(-\tfrac{1}{2}t^2)dt, \qquad (3.8)$$

where

$$F_{12} = \frac{\sqrt{1-g_{12}}}{\sqrt{1+g_{12}}} \frac{1+g_{12}-g_{13}-g_{23}}{\sqrt{|G|}}, \qquad (3.9)$$

and $|G| = 1 - g_{12}^2 - g_{13}^2 - g_{23}^2 + 2g_{12}g_{13}g_{23}$. Similar expressions can be derived for $\partial p_3^T/\partial g_{13}$ and $\partial p_3^T/\partial g_{23}$. Defining $A_{ij} = \partial p_3^T/\partial g_{ij}$ we have therefore

$$p_3^T(g_{12}, g_{13}, g_{23}) = g_{12} \int_0^1 A_{12}(tg_{12}, tg_{13}, tg_{23})dt$$

$$+ g_{13} \int_0^1 A_{13}(tg_{12}, tg_{13}, tg_{23})dt$$

$$+ g_{23} \int_0^1 A_{23}(tg_{12}, tg_{13}, tg_{23})dt. \qquad (3.10)$$

The truncated three point correlation function p_3^T is related to the p_3 by the expression

$$p_3(g_{12}, g_{13}, g_{23}) = p_3^T(g_{12}, g_{13}, g_{23}) + pp_2(g_{12})$$

$$+ pp_2(g_{13}) + pp_2(g_{23}) - 2p^3. \qquad (3.11)$$

To examine the limit $r_{12} \to 0$ ($g_{12} \to 1, g_{23} \to g_{13}$) set $f(g_{13}) = p_3^T(1, g_{13}, g_{13})$ then $df(g_{13})/dg_{13} = (1 - 2p)dp_2(g_{13})/dg_{13}$ and $f(0) = 0$ implying $p_3^T(1, g_{13}, g_{13}) = (1-2p)[p_2(g_{13}) - p^2]$ as it should. (Similarly in the other limits.) The x-ray spectra of these materials can be calculated from p_2 [22,20,37] and hence they can be related to physical composites. Furthermore it has been shown that the surface to volume ratio is given by [22,36]

$$\frac{S}{V} = \frac{2}{\pi} e^{-\frac{1}{2}\alpha^2} \sqrt{\frac{1}{3}\langle k^2 \rangle}. \qquad (3.12)$$

As the evaluation of the integrals in Eqs. (3.5) and (3.11) is computationally intensive it is useful to derive various approximations. Rigorous approximations for p_2 for the cases $|\alpha| \ll 1$ and $|\alpha| \gg 1$ are derived in Appendix A. A useful nonrigorous approximation to p_{123}^T can be developed by requiring that the approximation have similar properties to the actual function for $r_{ij} \gg 1$ and satisfy the known consistency conditions in various limits [40]. Using the compact notation $p_{ij}^T = p_2(g_{ij}) - p^2$ and $p_{ijk}^T = p_3^T(g_{ij}, g_{ik}, g_{jk})$ we have ($r_{ij} \gg 1$)

$$p_{ij}^T \propto g_{ij}, \qquad (3.13)$$

$$p_{123}^T \propto g_{12}g_{13} + g_{12}g_{23} + g_{13}g_{23}. \qquad (3.14)$$

Using this information, and including a higher order term for consistency $[p_3(r_{12}, r_{12}, 0) = p_2(r_{12})]$, we construct

$$p_{123}^T \approx \frac{1-2p}{2p(1-p)} \left(p_{12}^T p_{13}^T + p_{12}^T p_{23}^T + p_{13}^T p_{23}^T \right)$$

$$- \frac{1-2p}{2p^2(1-p)^2} p_{12}^T p_{13}^T p_{23}^T. \qquad (3.15)$$

We note that this approximation has a maximum absolute error of $O(10^{-3})$ for the materials considered here. As such it is an order of magnitude better than a previously suggested approximation [47] $p_3(r_{12}, r_{13}, r_{23}) \approx p_2(u)p_2(v)/p$ where u and v are the smallest, and next to smallest, values of r_{12}, r_{13}, and r_{23}.

IV. DETERMINATION OF ζ_1

Actual calculations of the microstructural parameter ζ_1 [Eq. (2.7)] have, to date, been for four classes of materials. Cellular materials [13,14], empirically measured physical composites [28], periodic arrays of spheres [48], and materials with spherical inclusions. In the latter class the cases studied include identical overlapping spheres [15,16] (the IOS model), identical hard spheres [49], and polydispersed spheres [25,2] (many of these results are summarized in Ref. [1]).

We now describe aspects of the computation of ζ_1 for several spectra of the Gaussian random interface (GRI) model. It can be shown that $\zeta_1 = \frac{1}{2}$ for $p = \frac{1}{2}$ [13,44,14] (see Appendix B) and that $\zeta_1 = 1 - \zeta_2$ where ζ_2 is the microstructure parameter associated with phase 2. As ζ_1 is dimensionless it must depend only on the ratios of the length scales associated with the spatial variables in the (dimensionless) correlation functions. That this should be so also follows from a simple dimensional analysis of the equations governing the electric field (no physical length scale is present). Henceforth we scale all spatial variables against a characteristic decay length without loss of generality.

We consider three types of media generated from Gaussian random fields. The field-field correlation functions and their corresponding spectra are as follows.

Model I:

$$g(r) = e^{-r}\frac{\sin \nu r}{\nu r}, \tag{4.1}$$

$$\rho(k) = \pi^{-2}\left[(1 - \nu^2 + k^2)^2 + 4\nu^2\right]^{-1}. \tag{4.2}$$

Here $\nu = 2\pi l_1/l_2$ with l_1 the decay length of the field and l_2 the characteristic domain size. When $r \gg 0$ the correlation functions arising from this model are similar to those considered in Refs. [22] ($\nu = 0$) and [20] ($\nu > 0$). Note that this model has an infinite surface to volume ratio since $\langle k^2 \rangle$ diverges, however for computational realizations of the model the ratio is finite (see Sec. V) and the model is well defined. However, it is interesting to study ζ_1 for this model to investigate the effect of interfacial roughness on effective properties.

Model II:

$$g(r) = e^{-r^2}, \tag{4.3}$$

$$\rho(k) = \frac{e^{-\frac{1}{4}k^2}}{(4\pi)^{\frac{3}{2}}}. \tag{4.4}$$

Model III:

$$g(r) = \frac{3\left(\sin \mu r - \mu r \cos \mu r - \sin r - r \cos r\right)}{r^3(\mu^3 - 1)}, \tag{4.5}$$

$$\rho(k) = \frac{3}{4\pi(\mu^3 - 1)}\left[H(\mu) - H(1)\right], \tag{4.6}$$

where $\mu = k_1/k_0$. Note that $\rho(k) \to \delta(k)$ as $\mu \to 1$ and the simple model used by Berk [35] is recovered.

To perform the integration (2.7) we use cylindrical coordinates (which damp the singularity at the origin), interchange the order of integration, and exploit the $r - s$ symmetry to give

$$\zeta_1 = \frac{9}{2pq}\int_{-1}^{1}\left(\int_{0}^{\infty}\int_{0}^{\frac{\pi}{4}} I(w,\phi,u)dwd\phi\right)P_2(u)du \tag{4.7}$$

with

$$I(w,\phi,u) = \frac{p\,p_3(r,s,t) - p_2(r)p_2(s)}{p^3 w \sin \phi \cos \phi}. \tag{4.8}$$

To elucidate the nature of the singularity in the integrand at $w = \phi = 0$ we consider w, ϕ (and hence r, s, and t) to be small and assume the form $g(r) \approx 1 - ar^n$ (where $n = 1, 2$ in accord with models I–III). Now for $p = \frac{1}{2}$ the numerator of the expression for I is given by

$$\frac{\sin^{-1}(g(t))}{8\pi} - \frac{\sin^{-1}(g(r))\sin^{-1}(g(s))}{4\pi^2} \approx \sqrt{2a}w^n\phi^n, \tag{4.9}$$

where we have used the results $\sin^{-1}(g(r)) \approx \frac{\pi}{2} - \sqrt{2ar^n}$, $r = w\cos\phi$, $s = w\sin\phi$, and $t = w\sqrt{1 - \sin 2\phi u}$. Therefore $I(w,\phi,u) \sim (w\phi)^{\frac{n}{2}-1}$ with $p = \frac{1}{2}$ and numerical analysis shows this scaling also holds for $p \neq \frac{1}{2}$. An integration rule which takes the singularity into account is employed. Note that for finite surface area to volume ratios $n = 2$. The number of abscissae in each of three integration ranges was increased until the third signif-

icant figure in the estimation of ζ_1 remained constant. The integration method was tested on the known correlation functions for the IOS model [23,15]. The results are in exact agreement (to the reported third significant figure) with those of Torquato and Stell [1,15] and agree to the second significant figure with the results of Berryman [16]. The calculation of the correlation functions in the integrand is done using a combination of iterative quadrature rules [50], the asymptotic results presented in Appendix A and the nonrigorous approximation for the truncated three point function (3.15). The latter is used whenever $1 - g < 10^{-5}$ since in this case the functions F_{ij} exhibit large derivatives and the quadrature rules converge too slowly. The accuracy sought in the application of each approximation is $O(10^{-6})$.

The results for each of the models is presented in Table I and plotted in Fig. 1 along side the results for the IOS model. Several comments on the qualitative relationship between ζ_1 for the GRI model and prior calculations can be made. Consider the expansion

$$\zeta_1 = \sum_{i=0}^{\infty} e_i p^i. \tag{4.10}$$

For a general class of materials with spherical inclusions it has been shown that $e_0 = 0$ [17,2]. If the inverse of these materials is considered (so that the correlation functions refer to the material surrounding the inclusion) or ellipsoidal inclusions are considered [17] then $e_0 > 0$ (see Appendix C). For the case of symmetric cell materials $e_0 = M \in [0,1]$ where $M = 0$ for spherical cells and $M = 1$ for platelike cells [7,13]. Another interesting feature of ζ_1 is that it is observed to be linear with p over a wide range [1,2]. Indeed for the symmetric cell model $e_1 = (1 - 2M)$ and $e_2, e_3 \cdots = 0$. By inspection of Fig. 1 we see that $e_0 > 0$ in qualitative agreement with the results for nonspherical inclusions which will occur in the GRI models. Also note that ζ_1 is very similar to the results for the symmetric cell model for some $0 < M < 1$

TABLE I. The microstructure parameter ζ_1 for various GRI models. Prior results for the identical overlapping sphere (IOS) model [1,15] and the symmetric spherical cell (SSC) model [13,7] are included for purposes of comparison.

|	Prior Results		GRI model			
p	SSC	IOS	I $\nu = 0$	I $\nu = 10$	II	III $\mu = 1.5$
0.01	0.01		0.269	0.193	0.099	0.060
0.05	0.05		0.293	0.217	0.160	0.105
0.1	0.1	0.056	0.319	0.248	0.210	0.150
0.2	0.2	0.114	0.366	0.309	0.291	0.237
0.3	0.3	0.171	0.411	0.372	0.363	0.324
0.4	0.4	0.230	0.456	0.436	0.432	0.411
0.5	0.5	0.290	0.500	0.500	0.500	0.500
0.6	0.6	0.351	0.544	0.564	0.568	0.588
0.7	0.7	0.415	0.589	0.628	0.636	0.675
0.8	0.8	0.483	0.634	0.691	0.709	0.763
0.9	0.9	0.558	0.681	0.752	0.790	0.850
0.95	0.95	0.604	0.707	0.783	0.840	0.895
0.99	0.99	0.658	0.731	0.807	0.901	0.940
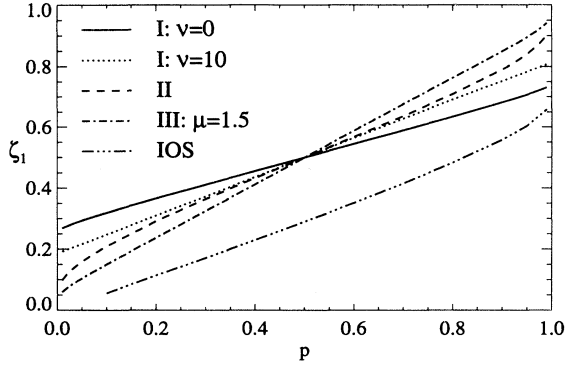
FIG. 1. The microstructure parameter ζ_1 vs p for the GRI models [Eqs. (4.1)–(4.6)] and the IOS model [1,15].

over a wide range of p. This discussion demonstrates the success of simple models of random media to capture the qualitative features of ζ_1 for the amorphous materials considered here.

Calculations of the related microstructure parameter η_1 which arises in bounds on the elastic properties of random composites are reported in Appendix E.

V. GENERATION OF FIELDS

For computational purposes we consider a T-periodic Gaussian random field [46] with a maximum wave number $K = 2\pi N/T$,

$$y_K(\mathbf{r}) = \sum_{l=-N}^{N} \sum_{m=-N}^{N} \sum_{n=-N}^{N} c_{lmn} e^{i\mathbf{k}_{lmn} \cdot \mathbf{r}}, \qquad (5.1)$$

where

$$\mathbf{k}_{lmn} = \frac{2\pi}{T}(l\mathbf{i} + m\mathbf{j} + n\mathbf{k}). \qquad (5.2)$$

For y_K real we require $c_{l,m,n} = \bar{c}_{-l,-m,-n}$ and as $\langle y_K \rangle = 0$ we set $c_{0,0,0} = 0$. For reasons which become clear below we also take $c_{lmn} = 0$ for $k_{lmn} = |\mathbf{k}_{lmn}| \geq K$.

With $c_{lmn} = a_{lmn} + i b_{lmn}$, a_{lmn} and b_{lmn} are random independent variables (subject to the conditions on c_{lmn}) with Gaussian distributions such that $\langle a_{lmn} \rangle = \langle b_{lmn} \rangle = 0$ and

$$\langle a_{lmn}^2 \rangle = \langle b_{lmn}^2 \rangle = \frac{1}{2} \rho_K(k_{lmn}) \left(\frac{2\pi}{T} \right)^3 \qquad (5.3)$$

with $\rho_K(k)$ the spectral density. The field-field correlation function g_K is given by

$$g_K(r_{12}) = \langle y_K(\mathbf{r}_1) \overline{y_K(\mathbf{r}_2)} \rangle \qquad (5.4)$$

$$= \sum_{-N}^{N} \sum_{-N}^{N} \sum_{-N}^{N} \langle c_{lmn} \overline{c_{lmn}} \rangle e^{i\mathbf{k}_{lmn} \cdot (\mathbf{r}_1 - \mathbf{r}_2)} \qquad (5.5)$$

$$\approx \int_0^K 4\pi k^2 \rho_K(k) \frac{\sin k |\mathbf{r}_1 - \mathbf{r}_2|}{k |\mathbf{r}_1 - \mathbf{r}_2|} dk. \qquad (5.6)$$

The last integral is obtained by taking N and T large, using Eq. (5.3) and recognizing that the summation is the approximation of a triple integral. Following a transformation to spherical coordinates we integrate over the angular variables to obtain (5.6). Since $g_K(0) = 1$ we define

$$\rho_K(k) = P^{-1} \rho(k), \quad P = \int_0^K 4\pi k^2 \rho(k) dk, \qquad (5.7)$$

where the $\rho(k)$ are defined in Sec. III. If in addition we take $K \to \infty$ then the conventional correlation function (and spectral density) are recovered. The Fourier expansion (5.1) is evaluated using a fast Fourier transform (FFT).

Consider materials derived from the field y_K [Eq. (5.1)] as discussed in Sec. III. Cross sections of the media for four different variants of the models are plotted in Figs. 2(a)–2(d). The large scale structure of the interface is determined by the terms in the expansion with small k while the small scale structure (ripples on the surface) are determined by the terms where k is large. A physical material will naturally contain a finite cutoff wavelength either imposed by the molecular size or by the manifestation of surface tension at the phase boundaries. This wavelength will then dictate the grid res-

(a) I: ν=0, K=18, T=4π   (b) I: ν=10, K=18, T=4π   (c) II: K=18, T=4π   (d) III: μ=1.5, T=4π

(e) I: ν=0, K=8, T=4π   (f) I: ν=10, K=32, T=π   (g) II: K=8, T=4π   (h) III: μ=1.5, T=8π
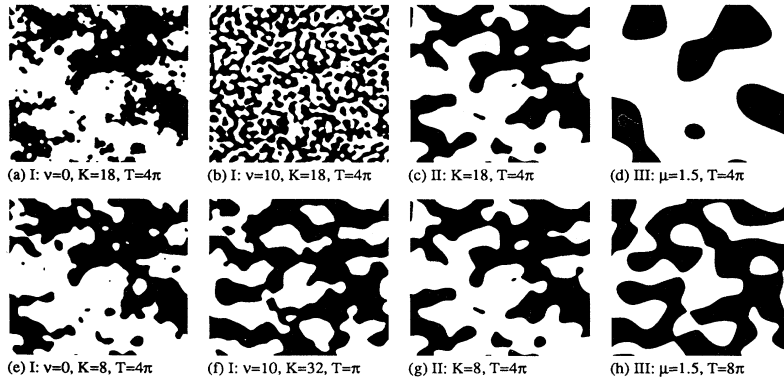
FIG. 2. Cross sections of the models generated at the same scale (a)–(d) and at the scale to be used in the simulations (e)–(h). The volume fraction $p = 0.5$ and each of the fields are generated using the same random number seed to clearly show the differences among the models. The parameters ν, μ, T, and K are discussed in the text.

TABLE II. The parameters used to generate the computational materials discussed in Secs. V and VII.

	Model	T	N	K
I	$\nu = 0$	4π	16	8
I	$\nu = 10$	π	16	32
II	–	4π	16	8
III	$\mu = 1.5$	8π	6	1.5

olution necessary to properly resolve the structure for simulational purposes. Conversely for this study the discretization $\Delta x = T/M$, where M is the number of grid points in the x direction, will restrict the choice of K. Thus $\Delta x \ll \lambda_{\min} = 2\pi/K$ or $N \ll M$. Another constraint is that $T \gg l_d$, where l_d is an effective decay length of the field defined by $g(l_d) = e^{-1}$. This must be so to ensure that the edges of the sample are uncorrelated to properly simulate an infinite random medium. For the approximation involved in determining g_K [Eq. (5.6)] to be accurate would require $T \gg 2\pi$, however in this study this constraint was found to be of less importance and is ignored.

The computational parameters used for each of the four variants of the models are given in Table II. Cross-sections of each of the materials are plotted in Figs. 2(e)–2(h) and the interface for models II and III are plotted in Figs. 3 and 4. To properly account for the effect of K for the computational models ζ_1 must be recalculated using $g_K(r)$. This is done using a look up table generated by numerical integration of (5.6) and an asymptotic expansion for large r (where the integral is costly to evaluate),

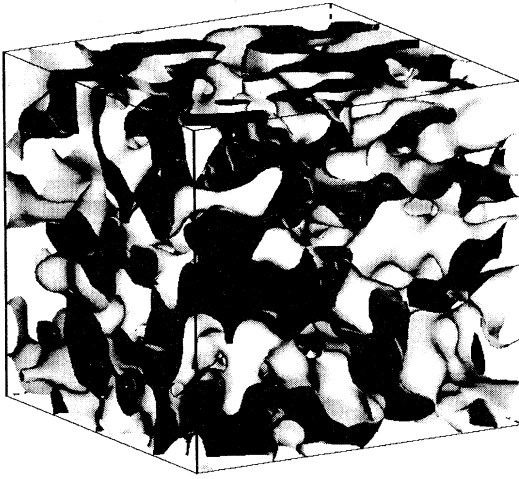$$g_K(r) = \frac{1}{P}g(r) - 4\pi K \rho_K(K) \cos Kr \frac{1}{r^2} + O\left(\frac{1}{r^3}\right). \quad (5.8)$$

FIG. 3. A plot of the interface $y_K(\mathbf{r}) = 0$ ($p = 0.5$) for model II. The parameters used to generate the field are $K = 8, T = 4\pi$. Note that the large scale structure of this model is similar to that of model I ($\nu = 0$) as can be seen by comparing Figs. 2(e) and 2(g).
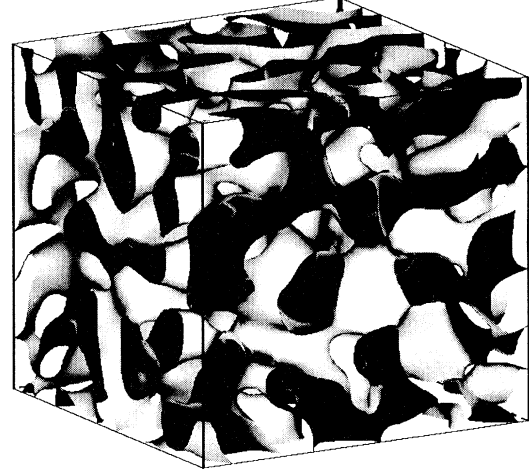

FIG. 4. A plot of the interface $y_K(\mathbf{r}) = 0$ ($p = 0.5$) for model III. The parameters used to generate the field are $\mu = 1.5, T = 8\pi$.

The function $g_K(r)$ for model I is plotted along with direct measurements of $\langle y(\mathbf{r}_1)y(\mathbf{r}_2)\rangle$ in Fig. 5. The agreement is seen to be very good. The values of ζ_1 for the computational models are presented in Table III. The effect of K on ζ_1 can be seen most clearly for model I where the surface area to volume ratio becomes arbitrarily large as K increases. The interfacial smoothing effect of imposing a finite cutoff (K) is shown in Figs. 2(a) ($K = 18$) and 2(e) ($K = 8$). This has the effect of decreasing (increasing) the magnitude of ζ_1 for $p < \frac{1}{2}$ ($p > \frac{1}{2}$) (compare Tables I and III). For small (and large) volume fractions this can be qualitatively explained by the fact that the inclusion phase of the model will be much rougher (and hence less "spherical") for $K = \infty$ than for $K = 8$ (see Appendix C). ζ_1 for model II is unchanged for finite K to the accuracy calculated here.
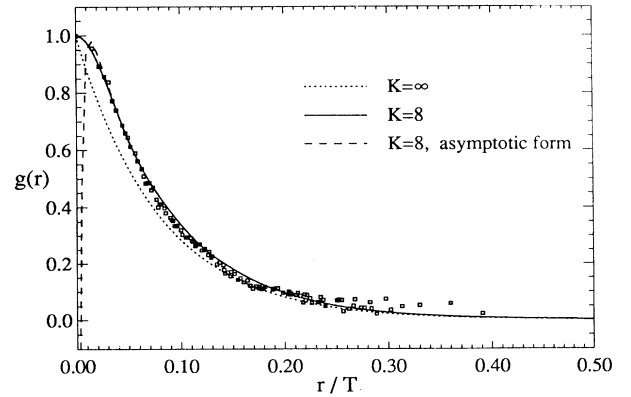

FIG. 5. The computational field-field correlation function $g_K(r)$ [Eq. (5.6)] for model I ($\nu = 0, K = 8$). The exact form (i.e., $K = \infty$) given by Eq. (4.1) and the asymptotic form, Eq. (5.8), are included for purposes of comparison. The data were measured from a single sample.

TABLE III. The microstructure parameter ζ_1 for the computational materials listed in Table II. The parameter K is the maximum wave number in the Fourier series. The relation $\zeta_1(p) = 1 - \zeta_1(1-p)$ can be used to determine ζ_1 for $p \geq 1/2$.

p	I $\nu = 0$ $K = 8$	I $\nu = 10$ $K = 32$	II $K = 8$
0.01	0.155	0.085	0.099
0.05	0.214	0.136	0.160
0.1	0.258	0.182	0.210
0.2	0.326	0.265	0.291
0.3	0.387	0.344	0.364
0.4	0.444	0.422	0.432

FIG. 6. The calculated values of $(\sigma_e)_M$ (solid circles) for varying volume fraction (p) and the exact data (open circles) [53] for the regular array of spheres. M is the discretization used in the finite difference scheme. The lines are linear least squares fits of the data over the range of M^{-1} where the data are approximately linear (generally $M^{-1} < 0.016$). σ_e is then given by the intercept of the lines with the axis $M^{-1} = 0$.

VI. SOLUTION OF THE LAPLACE EQUATION

There are a variety of different methods of simulating the effective conductivity of an inhomogeneous medium. These include direct solution of the partial differential equations governing the potential ϕ [51], Brownian motion algorithms [9–11], Fourier methods [52], and other techniques [12].

We solve Laplace's equation with the charge conservation boundary conditions discussed in Sec. II in a cube of side length T using M^3 nodes. A potential of ϕ_1 and ϕ_0 are applied on the faces $z = 0$ and $z = T$ and periodic boundary conditions are imposed on the four faces parallel to the direction of the current to model a sample of infinite extent in the x and y directions. A finite difference scheme is used to approximate the field and is solved using a conjugate gradient (CG) method. In Appendix D we discuss the efficient implementation of the algorithm on a parallel computer. The z components of the current and the field are then used in Eq. (2.4) to determine $(\sigma_e)_M$. The convergence criterion of the CG solver is decreased until the third significant figure of $(\sigma_e)_M$ remained constant. To estimate the continuum value of σ_e we assume that $\sigma_e \approx (\sigma_e)_M + a_1 M^{-1}$ and fit a line (using least squares) to several values of $(\sigma_e)_M$ vs M^{-1}. The intercept of this line with the axis $M^{-1} = 0$ then provides σ_e.

Before proceeding to the random media we simulate the effective conductivity of a regular array of spheres of conductivity $\sigma_1 = 10$ in a matrix of conductivity $\sigma_2 = 1$. Exact results for this model have been calculated by McKenzie et al. [53] and the model has been used by previous authors [10,12] to test the accuracy of their algorithms. For computational purposes the array contains four spheres in the z direction (using six spheres changes σ_e by less than 1%). The values of $(\sigma_e)_M$ for increasing concentration are plotted along with the lines of best fit used to estimate σ_e in Fig. 6. The graph demonstrates the necessity of extrapolating the data to $M^{-1} \to 0$. The results for σ_e are presented in Table IV. The error is less than 1% for $p \leq 0.4$ but increases to around 3% at $p = 0.5$ near the percolation threshold $p_c \approx 0.52$. For the random media it was found that computing $(\sigma_e)_M$ at more than two values of M did not significantly alter the estimation of σ_e.
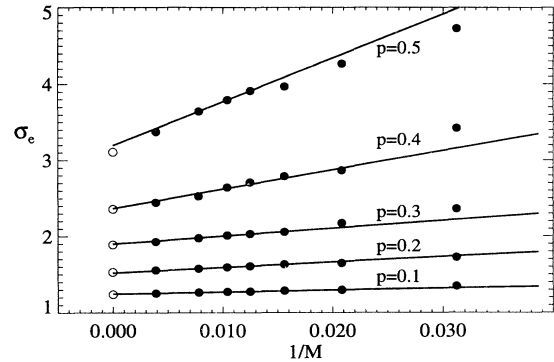
For the random media we must consider how to assign the conductivity of a bond lying between two nodes which lie in different phases. Let $y_{i,j}$ and $\sigma_{i,j}$ be the respective values of the field and the conductivity at two such neighboring nodes. There are three obvious ways of determining σ_{ij}. Defining $a = (\alpha - y_i)/(y_j - y_i)$ we can choose $\sigma_{ij} = a\sigma_j + (1-a)\sigma_i$ (as if the portions of the volume element associated with the bond are like conductors in *parallel*), $\sigma_{ij} = [a/\sigma_j + (1-a)/\sigma_i]^{-1}$ (as if in *series*) or $\sigma_{ij} = \sigma_1$ or σ_2 as $(y_i + y_j)/2 > \alpha$ or $(y_i + y_j)/2 < \alpha$ (a simple field *average*). In Fig. 7 we show the effect of using these rules for two samples of material I generated with $N = 4, 16$. For a given discretization (M) a large difference in σ_e occurs depending on the rule employed. However, extrapolation to $M^{-1} = 0$ demonstrates remarkably well that the choice is immaterial. As the simple averaging rule provides the least error for given M it will be used. Finally, for a given volume fraction we use the bisection method to calculate the value of the level cut parameter α' such that $\langle \sigma \rangle = p\sigma_1 + q\sigma_2$ (where

TABLE IV. Comparison of the extrapolated finite difference simulations with the exact results [53] for a simple cubic array of spheres of conductivity $\sigma_1 = 10$ in a matrix of conductivity $\sigma_2 = 1$. The Brownian motion simulations of Kim and Torquato [10] and the simulations of Bonnecaze and Brady [12] are also included. The spheres touch at $p = \pi/6 \approx 0.52$.

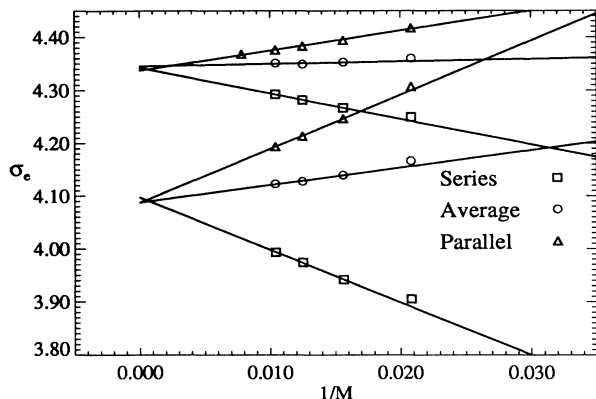| p	Exact Results	Finite Diff. This work	Relative Error	Kim-Torquato	Bonnecaze-Brady
0.1	1.24	1.25	0.8%	1.24	1.24
0.2	1.53	1.52	0.7%	1.53	1.53
0.3	1.89	1.90	0.5%	1.89	1.87
0.4	2.36	2.37	0.4%	2.36	2.29
0.5	3.11	3.19	2.6%	3.13	2.80

FIG. 7. The values of $(\sigma_e)_M$ for sample Gaussian media using the three different rules for assigning a conductivity to each bond (see text). Note that large variations in $(\sigma_e)_M$ occur for given M if different rules are employed. However, the choice is seen to be immaterial when the data are extrapolated to $M^{-1} \to 0$.
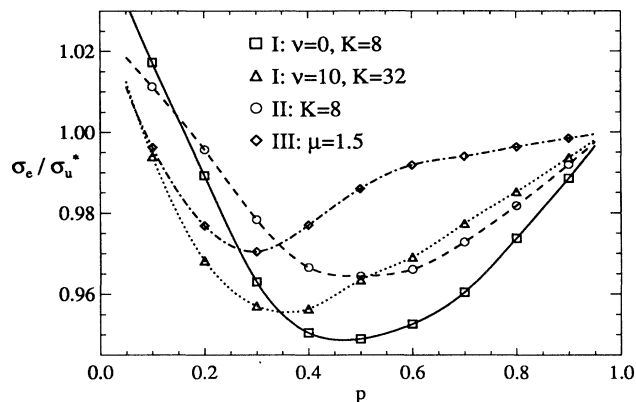

FIG. 8. The data for four different GRI models with conductivities $\sigma_1 = 10$ and $\sigma_1 = 1$. The data are normalized against the BM upper bound [Eq. (2.6)] with $\zeta_1 = p$ to highlight the differences between the models. The curves are spline fits of the data.

$\langle \ \rangle$ refers to bond averaging). This substantially reduces the statistical fluctuations in σ_e compared to using the theoretical value of α determined from Eq. (3.4).

VII. SIMULATION RESULTS

We simulate the effective conductivity for the four GRI models listed in Table II for a range compositions. As we are dealing with finite sized samples we report σ_e as the average over a number of different realizations of the materials. Error bars, which represent 95% confidence limits on the results, are equal to twice the standard error. The samples are examined at three different contrast values:

$\sigma_{1,2} = 10, 1$, $\sigma_{1,2} = 50, 1$, and $\sigma_{1,2} = 1, 0$. Previous authors [10,11,54] have considered media with $\sigma_{1,2} = \infty, 1$ but this is not possible using the methods discussed here.

The results for the case $\sigma_{1,2} = 10, 1$ are presented in Table V and plotted in Fig. 8 for $p \in [0.1, 0.9]$. To obtain the data five samples of each model with discretizations using $M = 64$ and $M = 96$ were considered. The results show little variation in σ_e (for fixed p) among the four different media. The maximum relative difference of 4.2% occurs at $p = 0.6$ between σ_e for model I ($\nu = 0$, $K = 8$) and model III ($\mu = 1.5$). As the differences are relatively small we restrict further attention to the latter two materials. The bounds calculated from Eqs. (2.6) and (2.8) using ζ_1 from Tables I and III are presented in Table VI and plotted along with the simulation data in Fig. 9, for $p \in [0.2, 0.8]$, and Fig. 10 for $p \in [0.86, 0.96]$. The latter figure illustrates very clearly that the upper bound discriminates between model I and III.

For the case $\sigma_{1,2} = 50, 1$ the results for model I ($\nu = 0$, $K = 8$) and model III ($\mu = 1.5$) are reported in Table VII and plotted along with relevant bounds in Fig. 11.

TABLE V. Simulations of σ_e for different GRI models with $\sigma_{1,2} = 10, 1$. The data for the IOS model [11] are included for purposes of comparison. The notation $x(y)$ implies $\sigma_e = x \pm y \times 10^{-2}$ with the error bars defined as 95% confidence limits. $y = 0$ implies $y < 0.5$.

p	I $\nu = 0$ $K = 8$	I $\nu = 10$ $K = 32$	II $K = 8$	III $\mu = 1.5$	IOS
0.1	1.36(1)	1.33(1)	1.35(1)	1.33(1)	
0.2	1.84(2)	1.80(2)	1.85(2)	1.82(3)	1.64
0.3	2.45(4)	2.43(2)	2.49(2)	2.47(3)	
0.4	3.19(5)	3.21(3)	3.24(3)	3.28(4)	2.73
0.5	4.06(6)	4.12(3)	4.12(2)	4.21(4)	
0.6	5.03(6)	5.12(2)	5.10(2)	5.24(6)	4.63
0.7	6.12(6)	6.23(1)	6.20(1)	6.33(6)	
0.8	7.33(4)	7.41(1)	7.39(1)	7.50(4)	7.11
0.86	8.13(3)			8.20(4)	
0.88	8.39(3)			8.46(4)	
0.90	8.65(2)	8.68(0)	8.67(2)	8.71(3)	
0.92	8.91(2)			8.97(3)	
0.94	9.18(2)			9.22(2)	
0.96	9.45(1)			9.48(1)	

TABLE VI. An example of the bounds calculated using Eqs. (2.6) and (2.8) and the data in Tables III (model I) and I (model III). The conductivity contrast is $\sigma_{1,2} = 10, 1$.

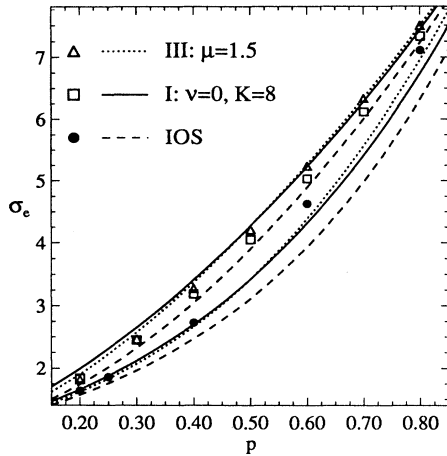|	I $K=8$, $\nu = 0$		III $\mu = 1.5$	
p	σ_l	σ_u	σ_l	σ_u
0.1	1.290	1.437	1.268	1.372
0.2	1.660	1.994	1.618	1.905
0.3	2.123	2.654	2.073	2.576
0.4	2.702	3.414	2.663	3.371
0.5	3.423	4.273	3.423	4.273
0.6	4.316	5.229	4.385	5.269
0.7	5.414	6.283	5.570	6.348
0.8	6.742	7.434	6.961	7.501
0.9	8.302	8.677	8.490	8.720

FIG. 9. Simulations and bounds for the effective conductivity of two models of random composite media generated from the GRI model for the case $\sigma_{1,2} = 10, 1$. The circular symbols represent data for the IOS model calculated by Kim and Torquato [11] and the bounds for the IOS model were evaluated by Torquato and Stell [15].

Again five samples of the media were considered with $M = 64$ and $M = 96$. Figure 11 shows very pronounced differences between the IOS model and GRI models. The results for the case $\sigma_{1,2} = 1, 0$ are given in Table VIII and plotted along with the upper bound (the lower bound vanishes) in Fig. 12. Five samples at discretizations $M = 48$ and $M = 64$ were considered.

There are several qualitative trends in the data which can be commented on. Note that for the first two contrasts considered σ_e of the GRI models is greater than that of the IOS model over the entire range of p. At low volume fractions this can be attributed to the fact
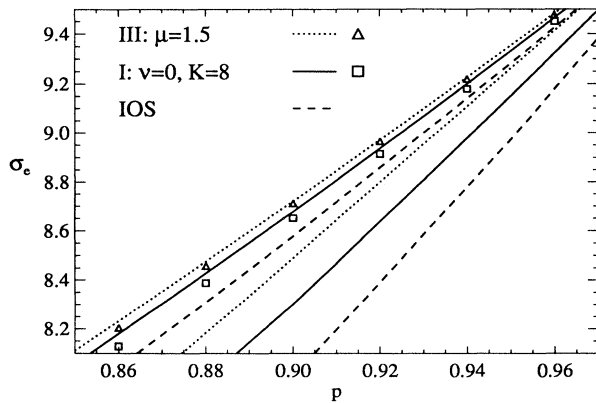
TABLE VII. Simulations of σ_e for the different Gaussian random media with $\sigma_1 = 50$ and $\sigma_2 = 1$. The IOS model data are from Ref. [11]. The error bars define 95% confidence limits.

	I $\nu = 0, K = 8$	III $\mu = 1.5$	IOS
0.1	1.88±0.08	1.69±0.06	
0.2	3.68±0.2	3.45±0.2	2.16
0.4	10.4±0.5	11.1±0.3	6.44
0.6	21.0±0.4	22.5±0.3	15.2
0.8	34.4±0.4	35.6±0.2	30.7

that the inclusions of the GRI models are qualitatively less spherical than those of the IOS model (see Appendix C). This can be clearly seen in Figs. 13 and 14 where the inclusions are plotted for each of the GRI models at $p = 0.07$ (the IOS model will contain predominantly spherical inclusions at this volume fraction). At high volume fractions the situation is reversed; the matrix phase of the IOS model is extremely ramified and hence σ_e is lower. Similarly near $p = 0, 1$ the small differences in σ_e for models I and III can be explained by the fact that the latter model has more spherical inclusions (compare Figs. 13 and 14). This behavior is consistent with the relative variations in ζ_1 for each of the three models as discussed in Appendix C. For midrange p the differences between the IOS and GRI models correspond to the fact that the more highly conducting regions of the latter are generally better connected than those of the IOS model. Again this difference can be anticipated from the relative behavior of the parameter ζ_1 for the two classes of models. However, this is not necessarily always so as can be seen by comparing the respective values of ζ_1 (Tables I and III) and σ_e (Table V) for models I and III at $p = 0.4$. In this case $\sigma_e^I < \sigma_e^{III}$ but $\zeta_1^I > \zeta_1^{III}$.

Note that the simulation data for the IOS model in the case $\sigma_{1,2} = 1, 0$ were obtained for insulating spheres in a matrix of unit conductivity. Therefore the microstructure of the conducting phase is generally better connected
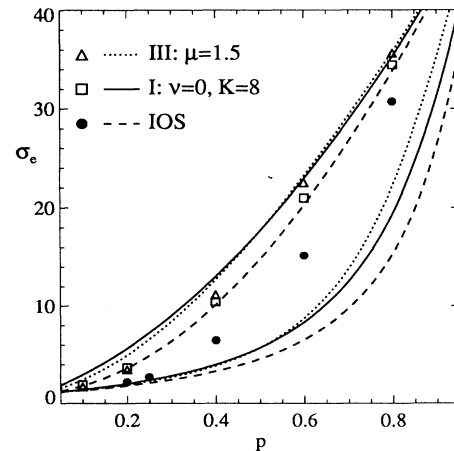

FIG. 10. Simulations and bounds for the effective conductivity of two models of random composite media generated from the GRI model for the case $\sigma_{1,2} = 10, 1$. The upper bound discriminates between the models in this range of p.

FIG. 11. As in Fig. 9 except $\sigma_1 = 50$ and $\sigma_2 = 1$.

TABLE VIII. Simulation of σ_e for different Gaussian random media with $\sigma_1 = 1$ and $\sigma_2 = 0$. The IOS model data are from Ref. [11]. The notation $x(y)$ implies $\sigma_e = x \pm y \times 10^{-3}$ with the error bars defined as 95% confidence limits. $y = 0$ implies $y < 0.5$.

p	I, $\nu = 0, K = 8$	III $\mu = 1.5$	IOS
0.1	0.002(2)	0.000(0)	0.022
0.2	0.027(6)	0.025(2)	0.076
0.3	0.080(3)	0.092(6)	0.160
0.4	0.166(12)	0.185(10)	0.248
0.5	0.264(10)	0.294(12)	0.346
0.6	0.383(9)	0.420(11)	0.461
0.7	0.521(12)	0.553(6)	0.593
0.8	0.670(7)	0.697(7)	0.714
0.9	0.830(3)	0.847(2)	0.855

FIG. 13. A plot of the interface $y_K(\mathbf{r}) = 1.48$ ($p = 0.07$) for model I. The parameters used to generate the field are $\nu = 0, K = 8, T = 4\pi$.

than the GRI models and the arguments pertaining to the qualitative variations in σ_e used above are reversed.

In all of the above cases the data lie between the appropriate bounds. Furthermore the upper bound is seen to provide a good estimate for σ_e for the GRI models for $p \geq 0.7$. This has been observed previously [1,55,11] for both high and low p (the latter case has not been considered in detail here). This fact provides evidence of the near optimality of bounds in these regions and a good confirmation of the techniques used in this paper (see Fig. 10 especially).

We have calculated the percolation threshold for model I and III using the algorithm of Skal et $al.$ [30]. In contrast to previous results [31] we found p_c to exhibit finite size effects and to depend on the spectrum. Averaging p_c over 10 fields at $M = 20, 32, 48, 64$ and extrapolating to $M = \infty$ we found $p_c \approx 0.07$ ($\alpha_c \approx 1.47$) for model I and $p_c \approx 0.13$ for model III ($\alpha_c \approx 1.13$). In the absence of theoretical percolation results for the GRI model it is interesting to discuss the threshold in terms of the tran-
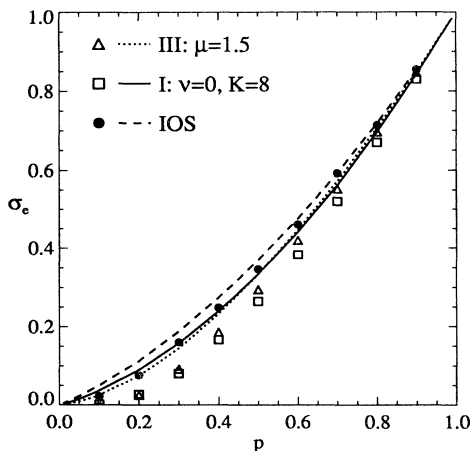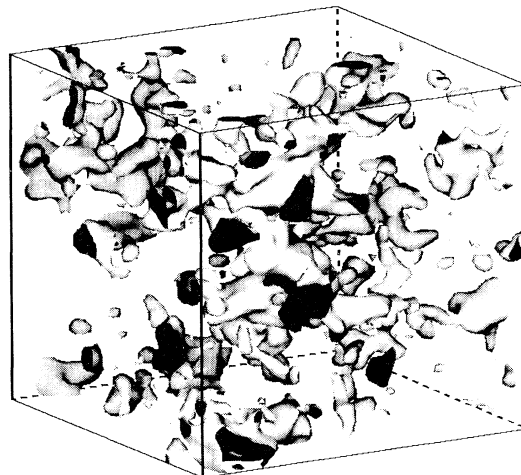
sition of the structures from elliptic to hyperbolic as p increases. The average Gaussian curvature $\langle K_G \rangle$ for the GRI models is given by [36]

$$\langle K_G \rangle = \frac{1}{6} \langle k^2 \rangle (\alpha^2 - 1). \tag{7.1}$$

Therefore the nature of the interface is dominated by inclusions of positive curvature (e.g., ellipsoids) for $|\alpha| > 1$ and is predominantly hyperbolic (e.g., bicontinuous) for $|\alpha| < 1$. The fact that $\alpha_c > 1$ indicates that connecting structures persist below the elliptic/hyperbolic transition as would be expected since $\langle K_G \rangle$ is an average quantity.

Finally it is interesting to discuss the surprisingly small variation in σ_e (and ζ_1) among the GRI materials. As can be seen in Figs. 2(a)–2(d) these materials appear to be
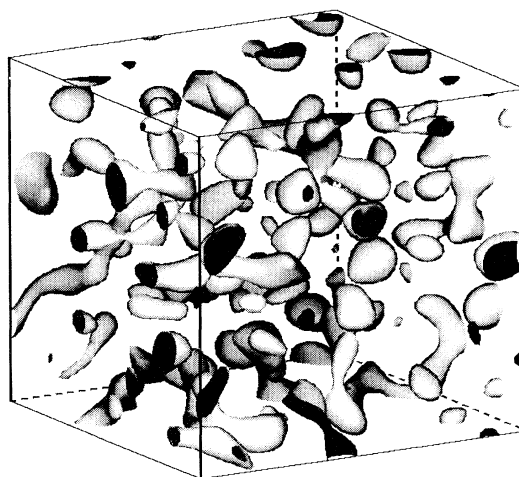

FIG. 12. As in Fig. 9 except $\sigma_1 = 1$ and $\sigma_2 = 0$.

FIG. 14. A plot of the interface $y_K(\mathbf{r}) = 1.48$ ($p = 0.07$) for model III. The parameters used to generate the field are $\mu = 1.5, T = 8\pi$.

very different when viewed at the same scale. However, the major qualitative differences are related to the effective decay length, and when the materials are viewed at a scale proportional to this length they appear to be remarkably similar as shown in Figs. 2(e)–2(h). Equivalently if the length parameters are retained in Eqs. (4.1)–(4.6) they can be tuned to achieve the latter group of figures at the same scale (without effecting σ_e). The remaining smaller qualitative differences account for the variation in σ_e observed.

VIII. CONCLUSION

We have investigated the effective conductivity of a two phase random composite material using bounding techniques and direct simulation. Our calculations of ζ_1 increase the classes of composites to which the bounds can be applied, while the simulation data can be used to assess predictive theories [56] and be compared with higher order bounds. The results also pertain to a variety of other effective properties of amorphous composites as discussed in Sec. II.

The bounds encompass all of the simulational data and the upper bound yields a reasonable estimate of σ_e for $p \geq 0.7$ ($\sigma_1 > \sigma_2$). Reasonably large differences in σ_e and ζ_1 are observed between the amorphous GRI models and the IOS model. This highlights the importance of incorporating microstructure effects in the calculation of the effective properties of composite materials. Conversely there is relatively little variation in σ_e among the GRI models as the major qualitative microstructural differences between the models are related to an effective decay length upon which σ_e is necessarily independent. We expect that other properties of such composites where no intrinsic field length scale is present (e.g., the elastic bulk and shear moduli) will show similar behavior.

It is clear that the Gaussian random interface model discussed here can serve as a useful "model" amorphous medium in the study of the effective properties of random composites. Furthermore the bounds and simulations can be related to physical composites by experimentally relating such systems to one of the theoretically known models. This could be done by comparing the spectra obtained from small angle scattering studies with that obtained from the 2-point correlation functions of each model. Or, more simply, by comparing images of the models with electron micrographs. Although such schemes are only approximate, our results indicate that the fine microstructural details are relatively unimportant in both the calculation of ζ_1 and the simulation of σ_e.

We note that the GRI model can be extended to the case of membranes and foams [35,56] and that higher order correlation functions can be calculated for use in more precise bounds. Random walker algorithms can be utilized to investigate the often studied scaling properties of σ_e near the percolation threshold.

ACKNOWLEDGMENTS

APPENDIX A: ASYMPTOTIC FORMS OF P_2

The two point function [Eq. (3.5)] can be expanded in powers of α to yield,

$$p_2(g) = \frac{1}{2\pi} \arcsin g + \frac{e^{-\frac{1}{2}\alpha^2}}{2\pi} \sum_{n=1}^{\infty} \frac{(-1)^n \alpha^{2n} a_n}{2^n n!} + p^2 \quad \text{(A1)}$$

with

$$a_n = \frac{2}{2n-1} \left[1 - \left(\frac{1-g}{1+g} \right)^{n-\frac{1}{2}} \right] - a_{n-1} \quad \text{(A2)}$$

and $a_0 = 0$. This expansion converges rapidly for small $|\alpha|$.

For the case $\alpha \gg 0$ we have (using successive integration by parts),

$$p \sim \frac{e^{-\frac{1}{2}\alpha^2}}{\sqrt{2\pi}\alpha} \left(1 + \sum_{n=1}^{\infty} \frac{(-1)^n 1 \times 3 \times \cdots \times (2n-1)}{\alpha^{2n}} \right). \quad \text{(A3)}$$

Special care must be taken to determine a practical expansion for p_2. A simple application of Watson's Lemma [57] yields a solution which does not possess the correct limiting behavior as $g \to 0$ and gives two different expansions for the cases $g = 1$ and $g < 1$. The first problem is dealt with by appropriately partitioning the integral, while the second necessitates a further transformation of variable, followed by an expansion in scaled parabolic cylinder functions (see for example Ref. [58]). Thus we write

$$p_2(g) = \frac{1}{2\pi} \left(\int_{-1}^{g} - \int_{-1}^{0} \right) \exp\left(-\frac{\alpha^2}{1+t} \right) \frac{dt}{\sqrt{1-t^2}} + p^2. \quad \text{(A4)}$$

In the second of these integrals we make the substitution $v = 1/(1+t) - 1$ to give

$$\frac{e^{-\alpha^2}}{2^{\frac{3}{2}}\pi} \int_0^{\infty} \frac{e^{-\alpha^2 v}}{(v+1)(v+\frac{1}{2})^{\frac{1}{2}}} dv \quad \text{(A5)}$$

which can be expanded using Watson's Lemma,

$$\frac{e^{-\alpha^2}}{2\pi} \left[\frac{1}{\alpha^2} - \frac{2}{\alpha^4} + \frac{7}{\alpha^6} + O\left(\frac{1}{\alpha^8} \right) \right]. \quad \text{(A6)}$$

This is just the expansion of p^2 which can be canceled from Eq. (A4). The remaining integral is put in a standard form by the substitution $v = 1/(1+t) - 1/(1+g)$,

$$p_2(g) = \frac{e^{-\frac{\alpha^2}{1+g}}}{2^{\frac{3}{2}}\pi} \int_0^\infty \frac{e^{-\alpha^2 v}}{(v + \frac{1}{1+g})(v + \frac{1}{2}\frac{1-g}{1+g})^{\frac{1}{2}}} dv. \quad \text{(A7)}$$

Note that the nature of the singularity of the integrand changes order as $g \to 1$ (this makes it impossible to generate an expansion for the full range of g using Watson's Lemma). To develop a uniform expansion for large α valid near $g = 1$ we make the further substitution,

$$v = \frac{1}{2}u^2 + \delta_g u, \quad \delta_g = \sqrt{\frac{1-g}{1+g}}, \quad \text{(A8)}$$

to give

$$\frac{e^{-\frac{\alpha^2}{1+g}}}{2\pi} \int_0^\infty \frac{e^{-\alpha^2(\frac{1}{2}u^2 + \delta_g u)}}{\left(\frac{1}{2}u^2 + \delta_g u + \frac{1}{1+g}\right)} du. \quad \text{(A9)}$$

In the usual way the nonexponential component of the integrand can be expanded in powers of u and integrated term by term to give,

$$p_2(g) \approx \frac{e^{-\frac{\alpha^2}{1+g}}}{2\pi} \left(\frac{1+g}{\alpha} T_1\left(\delta_g \alpha\right) - \frac{(1+g)^2}{\alpha^2} \delta_g T_2\left(\delta_g \alpha\right)\right.$$
$$\left. + \frac{(1-2g)(1+g)^2}{2\alpha^3} T_3\left(\delta_g \alpha\right)\right) \quad \text{(A10)}$$

where

$$T_n(z) = \int_0^\infty e^{-zs - \frac{1}{2}s^2} s^{n-1} ds = \Gamma(n)e^{\frac{1}{4}z^2} U(n - \frac{1}{2}, z). \quad \text{(A11)}$$

$U(a,z)$ is a parabolic cylinder function [59]. Two simple checks can be made on this expansion. For $g = 1$ we have $T_n(0) = 2^{n/2-1}\Gamma(\frac{n}{2})$ which, when substituted in (A10), gives the expansion of p. For $g < 1$ we again employ Watson's Lemma to determine the asymptotic expansion,

$$T_n(z) = \sum_{j=0}^\infty \frac{(-1)^j \Gamma(n+2j)}{j! 2^j z^{n+2j}}. \quad \text{(A12)}$$

Now taking $g = 0$ in (A10) and using this expansion gives the asymptotic form of p^2 as it should. The expansions for the case $\alpha \ll 0$ ($p \approx 1$) are simply, $p = 1 - AE_1$ and $p_2(g) = 2p - 1 + AE_2$, where AE_1 and AE_2 are the asymptotic expansions given by (A3) and (A10), respectively, with α replaced by $|\alpha|$. Note that Berk [35,37] has derived a formal series representation of p_2 valid for all α, however the convergence of the series is slow for $g \approx 1$ and not guaranteed at $g = 1$.

APPENDIX B: PROOF OF $\zeta_1 = \frac{1}{2}$ FOR $P = \frac{1}{2}$

In Brown's formulation the parameter ζ_1 arises as the limit as $\epsilon \to 0$ of the integral

$$\zeta_1 = \frac{9}{2pq} \int_\epsilon^\infty \frac{dr}{r} \int_\epsilon^\infty \frac{ds}{s} \int_{-1}^1 du P_2(u) f(r,s,t) \quad \text{(B1)}$$

where f is the term in brackets of Eq. (2.7). Now by

taking $p = \frac{1}{2}$ in Eq. (3.11) we have $f = p_2^T(t)/2 - 2p_2^T(r)p_2^T(s)$. Note that the integral of the second term vanishes since it does not depend on u and $\int_{-1}^1 P_2(u)du = 0$. Therefore after making the substitution $t^2 = r^2 + s^2 - 2sru$ Eq. (B1) becomes

$$\zeta_1 = 9 \int_\epsilon^\infty dr \int_\epsilon^r ds \int_{r-s}^{r+s} p_2^T(t)h(r,s,t)dt, \quad \text{(B2)}$$

where $h(r,s,t) = t(sr)^{-4}[\frac{3}{4}(t^2 - s^2 - r^2)^2 - r^2t^2]$. Interchanging the order of integration results in

$$\zeta_1 = 9\left(\int_0^{2\epsilon} + \int_{2\epsilon}^\infty\right) p_2^T(t) \int_\epsilon^\infty ds \int_s^{t+s} h dr$$
$$- 9\int_{2\epsilon}^\infty p_2^T(t) \int_\epsilon^{t/2} ds \int_s^{t-s} h dr, \quad \text{(B3)}$$

and carrying out the straightforward integrations over r and s leads to

$$\zeta_1 = 9\int_0^{2\epsilon} p_2^T(t) \left(\frac{2t^2}{3\epsilon^3} - \frac{t^3}{2\epsilon^4} + \frac{t^5}{24\epsilon^6}\right) dt. \quad \text{(B4)}$$

Now by taking $\epsilon \to 0$ and using the fact that $p_2^T(0) = \frac{1}{4}$ gives $\zeta_1 = \frac{1}{2}$.

APPENDIX C: RELATIONSHIP BETWEEN σ_E, ζ_1, AND SHAPE AT LOW P

Consider the small concentration approximation [60] to σ_e for the case of randomly distributed and oriented spheroids with axial ratios $A, A, 1 - 2A$,

$$\sigma_e = \sigma_2 + \frac{1}{3}p(\sigma_1 - \sigma_2)z(\sigma_1, \sigma_2, A) + O(p^2), \quad \text{(C1)}$$

where

$$z = \frac{2\sigma_2}{\sigma_2 + A(\sigma_1 - \sigma_2)} + \frac{\sigma_2}{\sigma_2 + (1 - 2A)(\sigma_1 - \sigma_2)}. \quad \text{(C2)}$$

With $A \in [0, 1/2]$ it can be easily shown that z has a unique minimum at $A = 1/3$ (spherical inclusions) and is monotonically increasing as $|A - 1/3|$ increases. Therefore with $\sigma_1 > \sigma_2$, σ_e will be higher the lower the sphericity of the inclusions (and conversely for $\sigma_2 > \sigma_1$). The same argument should qualitatively hold for arbitrary shapes. To see how this relates to ζ_1 we match the terms of the expansions of Eq. (C1) and Eq. (2.6) to order p and $(\sigma_1 - \sigma_2)^3$ which gives [13,17] $\zeta_1 = (1 - 3A)^2 + O(p)$. Thus ζ_1 will be higher for less spherically shaped inclusions.

APPENDIX D: IMPLEMENTATION OF THE FINITE DIFFERENCE SCHEME

The finite difference scheme (see, for example, Ref. [50]) for the equations and boundary conditions discussed in Sec. II leads to a system of simultaneous equations for the value of the potential at each of the interior nodes (including those on lateral faces if we define ϕ to be periodic in the x and y directions). For each such node u we have

$$\sum_{v \in nn} \sigma_{uv}(\phi_u - \phi_v) = 0, \qquad (D1)$$

where nn is the set of nearest neigbors of node u and σ_{uv} is the conductivity of the bond lying between nodes u and v. Conventionally these equations are cast as a matrix equation with ϕ and the boundary conditions as one dimensional matrices (vectors) [50]. On a parallel computer it saves coding and implementation time to retain the potential $\phi_{i,j,k}$ as a 3D matrix. Define A as the operator which performs the operations defined on the left hand side of (D1) for interior nodes and $A\phi \equiv \phi$ on the nodes where Dirichlet conditions are to be applied. Also define b as a 3D matrix containing the boundary conditions on the field ($b_{i,j,1} = \phi_1$, $b_{i,j,M} = \phi_0$ for all i, j and $b = 0$ elsewhere). Then solving the system of equations for ϕ is equivalent to minimizing $\| A\phi - b \|_2$, which can be done using a conjugate gradient method which handles vectors of general dimension.

APPENDIX E: CALCULATION OF THE MICROSTRUCTURE PARAMETER η_1

Three point bounds have also been derived for the elastic bulk and shear moduli [5–7,61] which can be expressed [7] in terms of ζ_1 and an additional parameter,

TABLE IX. The microstructure parameter η_1 which arises in bounds on the elastic bulk and shear moduli (see Appendix E) for selected Gaussian media. Data for the IOS model [1,62] are included for purposes of comparison.

p	IOS	I $\nu = 0$ $K = \infty$	I $\nu = 0$ $K = 8$	III $\mu = 1.5$
0.1	0.075	0.276	0.213	0.106
0.2	0.149	0.333	0.291	0.197
0.3	0.224	0.388	0.362	0.294
0.4	0.295	0.444	0.432	0.396
0.5	0.367	0.500	0.500	0.500
0.6	0.439	0.556	0.568	0.604
0.7	0.512	0.612	0.637	0.706
0.8	0.583	0.667	0.709	0.803
0.9	0.658	0.724	0.787	0.894

$$\eta_1 = \frac{5}{21}\zeta_1 + \frac{150}{7pq}\int_0^\infty \frac{dr}{r}\int_0^\infty \frac{ds}{s}\int_{-1}^1 du P_4(u)$$
$$\times \left(p_3(r,s,t) - \frac{p_2(r)p_2(s)}{p} \right). \qquad (E1)$$

We have calculated η_1 for several different GRI models and tabulated (see Table IX) it along with data for the IOS model. Qualitatively the results are similar to those for ζ_1 and we expect the differences in the effective shear and bulk moduli among the GRI models to be similar to those observed for the conductivity case.

[1] S. Torquato, Appl. Mech. Rev. **44**, 37 (1991).

[2] J. F. Thovert, I. C. Kim, S. Torquato, and A. Acrivos, J. Appl. Phys. **67**, 6088 (1990).

[3] Z. Hashin and S. Shtrikman, J. Appl. Phys. **33**, 3125 (1962).

[4] M. Beran, Nuovo Cimento **38**, 771 (1965).

[5] M. Beran and J. Molyneux, Quart. Appl. Math. **24**, 107 (1966).

[6] J. J. McCoy, *Recent Advances in Engineering Science* (Gordon and Breach, New York, 1970), pp. 235–254.

[7] G. W. Milton, Phys. Rev. Lett. **46**, 542 (1981).

[8] G. W. Milton, J. Appl. Phys. **52**, 5294 (1981).

[9] I. C. Kim and S. Torquato, J. Appl. Phys. **68**, 3892 (1990).

[10] I. C. Kim and S. Torquato, J. Appl. Phys. **69**, 2280 (1991).

[11] I. C. Kim and S. Torquato, J. Appl. Phys. **71**, 2727 (1992).

[12] R. T. Bonnecaze and J. F. Brady, Proc. R. Soc. London, Ser. A **430**, 285 (1990).

[13] M. N. Miller, J. Math. Phys. **10**, 1988 (1969).

[14] G. W. Milton, J. Mech. Phys. Solids **30**, 177 (1982).

[15] S. Torquato and G. Stell, J. Chem. Phys. **79**, 1505 (1983).

[16] J. G. Berryman, J. Phys. D **18**, 585 (1985).

[17] S. Torquato, J. Chem. Phys. **83**, 4776 (1985).

[18] P. B. Corson, J. Appl. Phys. **45**, 3165 (1974).

[19] R. Li and K. Sieradzki, Phys. Rev. Lett. **68**, 1168 (1992).

[20] M. Teubner and R. Strey, J. Chem. Phys. **87**, 3195 (1987).

[21] P. Pieruschka and S. Marčelja, Langmuir **10**, 345 (1994).

[22] P. Debye, H. R. Anderson, and H. Brumberger, J. Appl. Phys. **28**, 679 (1957).

[23] H. L. Weissberg, J. Appl. Phys. **34**, 2636 (1963).

[24] M. Doi, J. Phys. Soc. Jpn. **40**, 567 (1976).

[25] G. Stell and P. A. Rikvold, Chem. Eng. Commun. **51**, 233 (1987).

[26] P. B. Corson, J. Appl. Phys. **45**, 3159 (1974).

[27] P. B. Corson, J. Appl. Phys. **45**, 3171 (1974).

[28] P. B. Corson, J. Appl. Phys. **45**, 3180 (1974).

[29] J. W. Cahn, J. Chem. Phys. **42**, 93 (1965).

[30] A. S. Skal, B. I. Shklovskii, and A. L. Éfros, Fiz. Tverd. Tela (Leningrad) **15**, 1423 (1973) [Sov. Phys. Solid State **15**, 961 (1973)].

[31] A. S. Skal, B. I. Shklovskii, and A. L. Éfros, Pis'ma Zh. Eksp. Teor. Fiz. **17**, 522 (1973) [JETP Lett. **17**, 377 (1973)].

[32] R. Zallen and H. Scher, Phys. Rev. B **4**, 4471 (1971).

[33] R. Blumenfeld and S. Torquato, Phys. Rev. E **48**, 4492 (1993).

[34] M. B. Isichenko, Rev. Mod. Phys. **64**, 961 (1992).

[35] N. F. Berk, Phys. Rev. Lett. **58**, 2718 (1987).

[36] M. Teubner, Europhys. Lett. **14**, 403 (1991).

[37] N. F. Berk, Phys. Rev. A **44**, 5069 (1991).

[38] P. Pieruschka and S. Marčelja, J. Phys. II France **2**, 235 (1992).

[39] P. Pieruschka and S. A. Safran, Europhys. Lett. **22**, 625 (1993).

[40] W. F. Brown, J. Chem. Phys. **23**, 1514 (1955).

[41] P. Weiner, Abh. Math. Phys. Kl. Konigl. Sach. Ges. **32**, 509 (1912).

[42] J. G. Berryman, J. Comput. Phys. **75**, 86 (1988).

[43] B. Lu and S. Torquato, Phys. Rev. B **42**, 4453 (1990).

[44] W. F. Brown, J. Math. Phys. **15**, 1516 (1974).

[45] S. Torquato and G. Stell, J. Chem. Phys. **82**, 980 (1985).

[46] M. C. Wang and G. E. Uhlenbeck, Rev. Mod. Phys. **17**, 323 (1945).

[47] H. L. Weissberg and S. Prager, Phys. Fluids **5**, 1390 (1962).

[48] R. C. McPhedran and G. W. Milton, Appl. Phys. A **26**, 207 (1981).

[49] S. Torquato and F. Lado, Phys. Rev. B **33**, 6428 (1986).

[50] W. H. Press, B. P. Flannery, S. A. Teukolsky, and W. T. Vetterling, *Numerical Recipes* (Cambridge University Press, Cambridge, 1986).

[51] R. B. Saeger, L. E. Scriven, and H. T. Davis, Phys. Rev. A **44**, 5087 (1991).

[52] L. C. Shen, C. Liu, J. Korringa, and K. J. Dunn, J. Appl. Phys. **67**, 7071 (1990).

[53] D. R. McKenzie, R. C. McPhedran, and G. H. Derrick, Proc. R. Soc. London, Ser. A **362**, 211 (1978).

[54] R. T. Bonnecaze and J. F. Brady, Proc. R. Soc. London, Ser. A **432**, 445 (1991).

[55] S. Torquato, J. Appl. Phys. **58**, 3790 (1985).

[56] A. P. Roberts and M. A. Knackstedt (unpublished).

[57] J. D. Murray, *Asymptotic Analysis* (Clarendon, Oxford, 1974), p. 19.

[58] N. Bleistein, Comm. Pure Appl. Math. **XIX**, 353 (1966).

[59] M. Abramowitz and I. A. Stegun, *Handbook of Mathematical Functions* (Dover, New York, 1972).

[60] J. A. Reynolds and J. M. Hough, Proc. Phys. Soc. (London) **70**, 769 (1957).

[61] G. W. Milton and N. Phan-Thien, Proc. R. Soc. London, Ser. A **380**, 305 (1982).

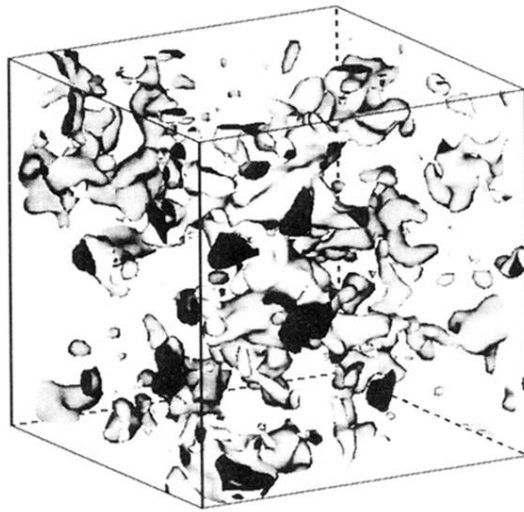[62] S. Torquato, G. Stell, and J. D. Beasley, Lett. Appl. Eng. Sci. **23**, 385 (1985).

FIG. 13. A plot of the interface $y_K(\mathbf{r}) = 1.48$ ($p = 0.07$) for model I. The parameters used to generate the field are $\nu = 0, K = 8, T = 4\pi$.
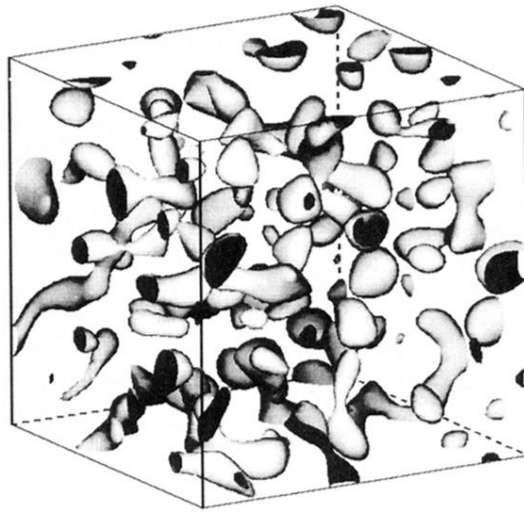
FIG. 14. A plot of the interface $y_K(\mathbf{r}) = 1.48$ ($p = 0.07$) for model III. The parameters used to generate the field are $\mu = 1.5, T = 8\pi$.
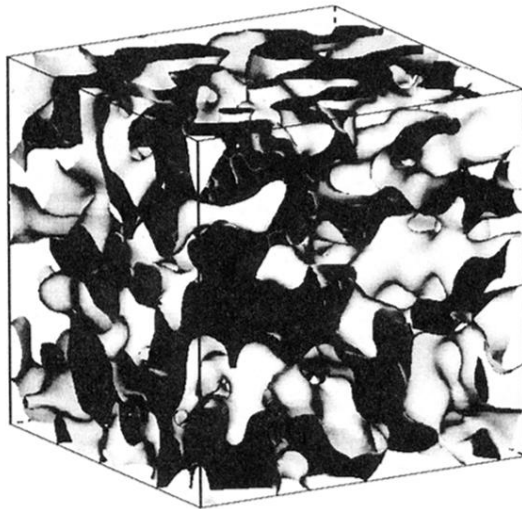
FIG. 3. A plot of the interface $y_K(\mathbf{r}) = 0$ ($p = 0.5$) for model II. The parameters used to generate the field are $K = 8, T = 4\pi$. Note that the large scale structure of this model is similar to that of model I ($\nu = 0$) as can be seen by comparing Figs. 2(e) and 2(g).

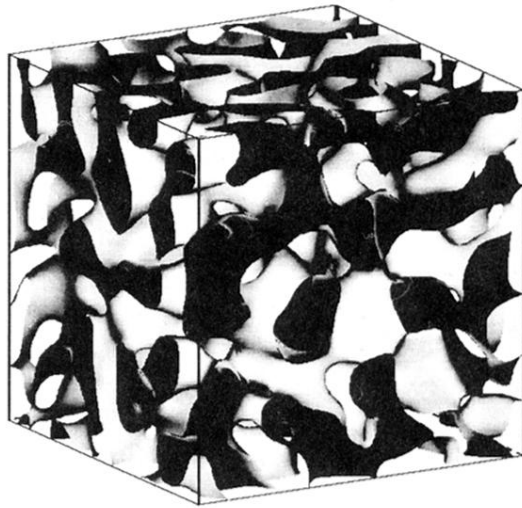FIG. 4. A plot of the interface $y_K(\mathbf{r}) = 0$ ($p = 0.5$) for model III. The parameters used to generate the field are $\mu = 1.5, T = 8\pi$.